REPORT DOCUMENTATION PAGE	*Form Approved* *OMB No. 0704-0188*

1. AGENCY USE ONLY *(Leave blank)*	2. REPORT DATE	3. REPORT TYPE AND DATES COVERED
	30 May 97	

4. TITLE AND SUBTITLE
COMPARISON OF SCINTILLATION DETECTION EFFICIENCIES OF DEPLETED URANIUM IN WOUNDS

5. FUNDING NUMBERS

6. AUTHOR(S)
SHELLEY ZUEHIKE

7. PERFORMING ORGANIZATION NAME(S) AND ADDRESS(ES)
COLORADO STATE UNIVERSITY
FORT COLLINS, COLORADO

8. PERFORMING ORGANIZATION REPORT NUMBER
97-052

9. SPONSORING/MONITORING AGENCY NAME(S) AND ADDRESS(ES)
DEPARTMENT OF THE AIR FORCE
AFIT/CI
2950 P STREET
WRIGHT-PATTERSON AFB OH 45433-7765

10. SPONSORING/MONITORING AGENCY REPORT NUMBER

11. SUPPLEMENTARY NOTES

12a. DISTRIBUTION AVAILABILITY STATEMENT
DISTRIBUTION STATEMENT A
Approved for public release
Distribution Unlimited

12b. DISTRIBUTION CODE

13. ABSTRACT *(Maximum 200 words)*

19970602 079

14. SUBJECT TERMS	15. NUMBER OF PAGES	16. PRICE CODE
	47	

17. SECURITY CLASSIFICATION OF REPORT	18. SECURITY CLASSIFICATION OF THIS PAGE	19. SECURITY CLASSIFICATION OF ABSTRACT	20. LIMITATION OF ABSTRACT

DTIC QUALITY INSPECTED 1

THESIS

COMPARISON OF SCINTILLATION DETECTION EFFICIENCIES OF DEPLETED URANIUM IN WOUNDS

Submitted by

Shelley Zuehlke

Department of Radiological Health Sciences

In partial fulfillment of the requirements

for the Degree of Master of Science

Colorado State University

Fort Collins, Colorado

Summer 1997

COLORADO STATE UNIVERSITY

May 16, 1997

WE HEREBY RECOMMEND THAT THE THESIS PREPARED UNDER OUR SUPERVISION BY SHELLEY ZUEHLKE ENTITLED COMPARISON OF SCINTILLATION DETECTION EFFICIENCIES OF DEPLETED URANIUM IN WOUNDS BE ACCEPTED AS FULFILLING IN PART REQUIREMENTS FOR THE DEGREE OF MASTER OF SCIENCE

Committee on Graduate Work

Thomas G. [illegible]

[illegible]

Shawki Ibrahim
Adviser

[illegible]
Department Head

ABSTRACT OF THESIS

COMPARISON OF SCINTILLATION DETECTION EFFICIENCIES
OF DEPLETED URANIUM IN WOUNDS

Depleted uranium (DU) has been used to reinforce military equipment and weapon systems due to its high density and metallurgical properties. During Desert Shield/Storm, some soldiers were wounded by fragments of depleted uranium metal which became imbedded in various locations in their bodies. The Army Radiation Research Office in Fort Belvoir, Virginia, requested assistance from Colorado State University in finding a portable and easily operated system for detecting depleted uranium in wounds. In a first step towards finding that detection system, a comparison of the relative efficiencies of three types of scintillation detectors was conducted. Tissue-equivalent cylindrical wound phantoms with varying activities of depleted uranium metal imbedded at varying depths were used to compare the efficiencies of a bismuth germanate (BGO) detector, a sodium iodide (NaI), and two identical wound probes with smaller sodium iodide crystals. The results show that the BGO detector had the highest efficiency (1.0×10^{-3}) and the lowest lower limit of detection (LLD) (0.156 μCi) for the shallow depth phantom. The BGO detector also had the highest efficiencies (1.7×10^{-3} and 5.8×10^{-4}) and the lowest LLDs (0.094 μCi and 0.276 μCi) for the medium and deep phantoms, respectively.

Shelley Zuehlke
Radiological Health Sciences Department
Colorado State University
Fort Collins, CO 80523
Summer 1997

ACKNOWLEDGEMENTS

I would like to thank the Air Force Institute of Technology for providing the funding for me to complete this masters degree program and the Army Radiation Research Office for providing me a research project from which I could complete a thesis. I would like to express my gratitude to my advisor, Dr. Shawki Ibrahim, and my committee members, Dr. David Rowan and Dr. Thomas Wilson, for their expertise and guidance on my thesis. I'd also like to thank Dr. John Campbell, who got me involved in my project and continued to assist me along the way.

I'd like to thank the department and other CSU faculty for their instruction and their imparting as much of their knowledge and expertise as my brain would allow. I appreciate and thank all the assistance and patience from the administrative staff - Julie Asmus, Joann Brown, Linda Jones, and Lee Wiedeman. Thanks also to Chuck Sampier, the department electronics specialist, for all his help as well.

As for my fellow graduate students, I couldn't have made it without them. They helped me not only in the academics, but helped me keep my sanity by being my friends and keeping me laughing.

I'd also like to thank the CSU Air Force Reserve Officer Training Corps, Detachment 90, for assisting me with Air Force matters during the past two years.

Finally, and most importantly, I'd like to thank my wonderful family for their unconditional love and support in everything that I do.

TABLE OF CONTENTS

LIST OF TABLES

LIST OF FIGURES

INTRODUCTION

During the Desert Shield/Desert Storm conflict in 1991, the U.S. military used weapons and weapon systems containing depleted uranium (DU). In 1992, the Director of Professional Service of the Office of the Surgeon General, United States Army, requested that the Armed Forces Radiobiology Research Institute (AFRRI) conduct a review of the scientific literature on the health effects of depleted uranium fragments imbedded in human tissue (AFRRI 93-2, 1993). The result of the review was documented in two 1993 technical reports which stated that approximately 22 soldiers, and possibly 13 more, received imbedded fragments of depleted uranium from injuries during Desert Shield/Desert Storm (AFRRI 93-2, 1993).

Depleted uranium's high density, approximately 18.9 grams per cubic centimeter (g/cm^3), and metallurgical properties make it desirable for armor and kinetic energy weapons capable of piercing armor (AEPI, 1995). The Department of Defense (DoD) primarily uses depleted uranium to reinforce the armor of military vehicles as well as in ordnances delivered from various weapons systems such as the M1 and M60 series tanks and the A-10 aircraft. The depleted uranium that the DoD uses is 99.8% by weight of ^{238}U, 0.20% of ^{235}U, 0.0003% of ^{236}U, and 0.001% of ^{234}U (AEPI, 1995). When DU-reinforced tanks are hit by armor piercing rounds and when DU munition rounds are fired, the metal from the tanks and the ordnances break apart into fragments called shrapnel. The metallic DU shrapnel can penetrate and disperse into various directions and materials. One of the main concerns is the possibility of soldiers receiving injuries from these pieces of shrapnel containing depleted uranium. As previously mentioned, during Desert Storm, soldiers received wounds containing pieces of imbedded DU shrapnel resulting from DU munitions hitting their vehicles and from pieces of the DU-reinforced tanks. The concerns of DU shrapnel include the physical injury from the fragment, the uranium metal chemical toxicity if absorbed

through blood, and the dose received from the radiation emitted from the fragment. Estimates of stochastic risks for each organ listed in ICRP 60 were calculated by the AFRRI for imbedded DU fragments ranging from 1 to 4 millimeters (mm). For the 4 mm fragment, the highest effective dose equivalent was to the thyroid and was estimated to be 1 mSv/yr or 100 mrem/yr (AFRRI 93-1, 1993). Another health risk of concern is the inhalation of uranium dioxide produced when depleted uranium is exposed to fire such as when DU munitions pierce DU-reinforced tanks.

The DoD, together with other organizations, are conducting long-term follow-ups for persons with known imbedded DU fragments (AFRRI 93-2, 1993). Since the possibility of a person receiving injury from depleted uranium fragments in future conflicts exists, part of the DoD monitoring protocols entail improving previous or developing new procedures for DU detection within wounds. Detecting depleted uranium in a wound can help physicians and other medical providers determine whether the fragment should be removed and what type of protocol should follow.

As a result of the AFRRI findings, the U.S. Army Radiation Research Office (ARRO) in Fort Belvoir, Virginia, requested assistance in finding a detector system useable in a field situation or hospital environment that can quickly screen for radioactivity within a DU-suspected wound. They requested that the Department of Radiological Health Sciences at Colorado State University compare several gamma scintillation detectors for their efficiency in detecting DU within wounds. The objectives of this research were:

1. Describe calibration protocols using depleted uranium in three wound phantoms constructed by Battelle, Pacific Northwest Laboratory.

2. Compare the efficiencies of three types of scintillation detectors in detecting gamma emissions from depleted uranium as a function of angle of the detector and depth of the DU source.

3. Provide detector performance data and recommendations to U.S. Army Radiation Research Office regarding the relative efficiencies of the detectors.

EXPERIMENTAL PROCEDURES AND METHODOLOGY

Depleted uranium and its daughter products are sources of alpha, beta, and gamma radiations. Since an imbedded depleted uranium fragment within a wound would be surrounded by tissue, the only radiation that would not be totally attenuated and prevented from external detection would be the gamma radiations. Depending on the depth of the fragment within the wound, the alpha and beta particles would most likely be stopped by the surrounding tissue of the wound and would therefore not be detectable by an external detector. The geometry, size, and activity of the depleted uranium fragment within the tissue are also factors in determining the efficiency of an external detector.

Uranium-238 decays by alpha emission to ^{234}Th, with a half life of 4.5×10^{9} years. Uranium-238 also emits a gamma of approximately 49.55 keV, with a very low frequency of emission. Thorium-234 decays by beta and gamma emission to ^{234m}Pa, with a half life of 24.1 days. Protactinium-234m decays by beta and gamma to ^{234}U, approximately 99.8% of the time, with a half life of 1.17 minutes. Protactinium-234m also decays by internal conversion to ^{234}Pa by beta and gamma 0.13% of the time. Protactinium-234 decays by beta and gamma to ^{234}U, with a half life of 6.7 hours. Because the half life of the parent (^{238}U) is much greater than the half lives of the daughters, there is sufficient time for ingrowth of the daughters and the activities of each are considered to be in secular equilibrium with ^{238}U. In this research, only the gammas from the first two daughters of ^{238}U contribute significantly to the total activity of the phantom sources, based on the half-lives and frequencies of emission (Table 1).

SCINTILLATION DETECTORS

Three types of inorganic scintillation detectors were compared in this research: a 2 x 2 inch bismuth germanate ($Bi_4Ge_3O_{12}$ - often referred to as BGO), Bicron model number 2M2BGO/2,

a 2 x 2 inch sodium iodide (NaI), Canberra/Bicron model number 802-3, and two identical 0.125 inch (diameter) x 0.5 inch Harshaw/Bicron sodium iodide wound probes. Both wound probes were used separately to make measurements and then the data were averaged in most cases to compare with the data collected by the BGO and NaI detectors.

The basic principles of operation of scintillation detectors involve the conversion of the kinetic energy of charged particles into detectable light. Gammas or photons are indirectly ionizing and can penetrate deeply into materials. Gammas have long paths through matter and the detection of gamma rays in a scintillation detector requires interactions within the crystal that transfer all or part of their energies to electrons.

Three primary interactions occur between the gammas and the crystal: 1) the photoelectric effect, 2) Compton scattering, and 3) pair production. The photoelectric effect is dominant for low-energy gammas, pair production is dominant for high energies, and Compton scattering is predominant at mid-range energies. The result of the photoelectric effect is the production of photoelectrons, sometimes followed by x-ray emission. The result of pair production is the creation of electron-positron pairs. Once the positrons lose enough kinetic energy, they will combine (annihilate) with normal electrons in the absorbing crystal, which results in the formation of two annihilation photons of the same energy (0.511 MeV). The result of Compton scattering is the formation of recoil electrons and scattered photons, where the energies of each depend upon the scattering angle.

As electrons slow down in the crystal, the energy they deposit is ultimately converted to excitations from which light is produced. The light photons are then reflected towards and fall on the photocathode of the photomultiplier tube (pmt). The photocathode converts low-energy photons into low-energy photoelectrons. The photoelectrons are accelerated by an electric field to the first dynode of the photomultiplier tube. When the electrons hit the dynode, secondary electrons are created. Secondary electrons are accelerated to the next dynode. Through a series of dynodes, the photomultiplier tube converts the low-energy photoelectrons into an electrical current that is large enough to be detected as a signal. At the last dynode, the current pulse is

passed through a resistor to produce a voltage pulse.

The magnitude of this voltage pulse is proportional to the kinetic energy which the electrons, resulting from the initial gamma interactions in the crystal, deposit in the scintillator. During each phase of operation, the number of light photons, photoelectrons, and secondary electrons are all directly proportional to the number of particles previously produced. Starting with the scintillator crystal, the number of visible light photons emitted is proportional to the energy deposited by the electrons in the crystal. Then, the number of photoelectrons produced at the photocathode is directly proportional to the number of light photons which fall on it and so on.

The voltage pulse can amplified by a linear amplifier and sent through a multichannel analyzer which measures the size of the voltage pulse and stores the information in a channel, based on the size of the pulse. The multichannel analyzer increments the number of counts in the appropriate channel individually. When all the pulses are displayed, they form a discrete (number of channels) gamma spectrum also called a differential pulse height spectrum.

In a differential pulse height spectrum, the total area under the spectrum represents the number of all pulses recorded, regardless of the amplitude of each pulse, and is used in determining the total efficiency of the counting system. A minimal pulse height is often set to discriminate between pulses from the gamma radiations and the pulses due to noise in the electronics.

Peaks will appear where full energy deposition events have occurred. These peaks are known as total absorption peaks, full energy peaks, or photopeaks. The number of full energy events can then be determined by integrating the area under the peak. In many experiments, the area under the peaks are used to determine a peak efficiency of a detection system rather than the total efficiency since the number of full energy events is not sensitive to electronic noise and scatter from surrounding objects (Knoll, 1979). Compton scattering events, where only partial energy deposition occur, show up on the spectrum at lower energies.

SOURCES OF DEPLETED URANIUM

Three wound phantoms, each containing a source of depleted uranium, were used in this research to determine the relative efficiencies of the three types of scintillation detectors in detecting depleted uranium. A fourth phantom, which does not contain depleted uranium, was used as a blank. The phantoms were constructed by Battelle, Pacific Northwest Laboratory, in Washington, and are shown in Figure 1.

Each of the phantoms is a polyacrylic cylinder. All four phantoms have a diameter of 17.78 cm but each one has a slightly different height. The material used to make the phantoms is a tissue-equivalent, two-component polyurethane that simulates average soft tissue as defined by ICRU Report 46 (Olsen, 1994). The density of the tissue-equivalent material is between 1.01 to 1.05 g/cm^3. Each phantom contains an actual piece of depleted uranium shrapnel from DU penetrator tank rounds. The shrapnel pieces were provided by the U.S. Army's Aberdeen Proving Grounds in Maryland to Battelle to construct the phantoms. On one side of each phantom, there is a target mark that indicates where the depleted uranium fragment is suspended within the phantom (Table 2).

The activity for each piece of depleted uranium within each phantom was calculated using the mass information provided by Battelle and the following equations:

$$N = \frac{m\ N_A}{A} \qquad (1)$$

where: N is the number of ^{238}U atoms
m is the mass of ^{238}U in grams
N_A is Avogardro's Number and
A is the atomic weight of ^{238}U

and

$$A = \lambda N \tag{2}$$

where: A is the activity of ^{238}U

λ is the ^{238}U decay constant and

N is the number of ^{238}U atoms

DETECTOR EFFICIENCY

In general, detector efficiency is a measure of how well the detector relates the number of pulses counted to the number of gammas incident upon the detector. The two classes of efficiency are absolute and intrinsic. Absolute efficiency is defined as the number of pulses recorded divided by the number of radiation quanta emitted by the source and it depends on the properties of the detector as well as the geometry of the counting system and source geometry (Knoll, 1979). The absolute efficiency will depend on the source-to-detector geometry because the number of gammas striking the detector from a point source will vary with the distance of the source to the detector face, the off-set of the source from the detector centerline, and the diameter of the detector. Some sources will self-absorb some of the radiations they emit. Intrinsic efficiency is defined as the number of pulses recorded divided by the number of quanta incident on the detector. The intrinsic efficiency depends mainly on the type of interacting material, the thickness of the material and the radiation energy.

Based on the x-rays and descriptions provided by Battelle, each phantom contains a different shaped DU source at a different depth within the phantom. Figure 2 is an x-ray of the DU fragment imbedded in the medium phantom. The masses and corresponding activities of DU in each phantom vary. These variations make it difficult to draw conclusions regarding the absolute efficiencies of each detector. DU is extremely dense and some emitted photons will be absorbed by the source itself and will not be detected. Since the geometries of the DU sources in the phantoms were not defined, the relative intrinsic efficiencies of each detector for a given phantom

were determined instead of absolute efficiencies.

SET-UP, CALIBRATION, AND DATA COLLECTION

The following equipment and instruments were used in this experiment:

1. Nucleus, Inc. Multichannel Analyzer (MCA)
2. Harshaw/Bicron Labtech single channel analyzer (scaler)
3. ^{137}Cs, ^{133}Ba, and ^{60}Co button calibration sources.
4. Ludlum photomultiplier tube (pmt) connector.

In order to determine the relative efficiencies of each of the detectors, several gamma spectra were collected using each detector for several counting periods. Each detector was connected to an MCA and was used to collect a long count spectra (16 to 20 hrs) and a short count spectra (10 minutes) from each source phantom, and a background spectra using the blank phantom.

Using sealed ^{137}Cs, ^{133}Ba, and ^{60}Co button sources, the MCA was energy calibrated using the 32 keV, 80.99 keV, 356 keV, 661.7 keV, and 1332.5 keV gamma and x-ray peaks of these sources. After separately calibrating each of the detectors using the photon energies of the button sources, the face of each detector was positioned against the surface of the phantoms where the targets are marked to collect the spectra as shown in Figure 3. When collecting data, the positions of the detectors on the phantoms were kept as consistent as possible by using a template to place the center of the detectors at the center of the source at the particular depth of the source. The distances between the detector face and each of the sources were from the outer surface of the phantom to where the source is suspended within each of the phantoms.

The purpose of counting for 16 and 20 hours was to establish a region of interest (ROIs) on the spectrum for each detector, using each phantom, where the signal-to-noise ratio was the greatest between the source and background. Increasing the counting time increases the precision of results, but may not always be possible or practical. Therefore, the purpose of the shorter count period of ten minutes was to compare the signal to noise ratios in the ROIs determined using the

long count data, given limited time, as would be expected in a field situation where a person might have a fragment of depleted uranium in a wound. Background spectra were collected with the same counting parameters using the blank phantom. The background spectra were subtracted from each DU spectrum collected from a source phantom. Spectra were collected from the wound probes separately to see how closely their responses were. Since their responses were similar, the data from each were averaged together and presented in the tables and graphs. From the ROIs, the efficiencies and the lower limits of detection (LLD) for each detector and for each phantom were calculated.

Variation in Positions Around Phantoms:

Spectra were also collected with the detector faces at various positions from the target mark to determine whether the angle of the detector from the source had an effect on the efficiency of the detector for the particular region of interest. Ten minute spectra were collected with each type of detector from five different positions around the surface of the phantoms. The five additional locations or positions were 1) directly opposite the target on the back of the phantom, 2) the left side of the target, 3) the right side of the target, 4) the top of the phantom, and 5) on the bottom of the phantom. The center of the detector faces were lined up with the center of the sources at the distances the sources are imbedded in the phantom as shown in Figure 4.

Side of Detectors:

MCA spectra were collected for ten minutes using the side of the BGO detector, NaI detector, and one of the wound probes positioned on the shallow phantom target surface to determine whether there was a significant difference in efficiency using the face versus the side of the detectors (Figure 5).

SINGLE CHANNEL ANALYZER (SCALER) DATA

Characteristic curves using the Bicron scaler were established to determine the operating voltages of each of the detectors . A sealed ^{137}Cs button source (~ 1 μCi) was used to create the curves. Counts were collected for one minute at incremental increases of the high voltage.

Reliability tests of the detectors connected to the scaler were conducted by collecting 30, one-minute counts at the operating voltages.

The scaler does not have an output from which the signal can be sent to an MCA. It can only indicate the number of counts and the count rate from a source. Therefore, the scaler was used to create net spectra from the plotted counts collected from the shallow and blank phantoms. The purpose of these measurements was to compare the manually created spectra with the spectra collected from the MCA and to try to optimize the settings on the scaler for DU detection.

A threshold setting was initially set at 0.02 volts on the scaler and counts were made in increasing 0.02 volt increments (window setting of 0.02V) for ten minute counting periods up to a threshold setting of one volt. This was accomplished using one of the wound probes with the shallow phantom as the source and the blank phantom as the background. Counts in ten minutes for each 0.02 volt window were also collected using the BGO and NaI only up to a window setting of 0.40 volts since the primary region of interest lies in the low energy portion of the spectra.

In addition, each detector was used to collect counts in ten minutes from the same six positions (including the target position) around each phantom as indicated in Figure 4. The lower threshold was set at 0.02 volts, which discriminated against most of the electronic noise, and no upper threshold. Background counts were subtracted to get the net counts for each of the six angles around the phantoms. From these net counts, the detection efficiencies were calculated.

RESULTS AND ANALYSIS

CHARACTERISTIC CURVES AND RELIABILITY TESTS

A one μCi sealed ^{137}Cs button source was used to create the characteristic curves for each detector. The operating voltage for the two wound probes ranged from 900 to 1000 V. The operating voltages for the NaI detector and BGO detector were 900 V and 1000 V, respectively. The reliability of the operating voltages were verified using a statistical method for counter reliability (Radiological Health Handbook, 1970).

GAMMA SPECTRA

Several peaks show up on the spectra as a result of the various gammas emitted from ^{238}U and its daughters. Peaks appear at energies of 63 and 93 keV from ^{234}Th, and 766 and 1001 keV from ^{234m}Pa when using the NaI and the BGO detectors. Peaks also appear at an energy approximating 1461 keV, which is from the gamma emitted by naturally occurring ^{40}K in the tissue-equivalent material. The lower energy gammas and x-rays were not as well resolved on either the long or short count spectra for all phantoms. Figure 6 shows the background spectra collected using each detector for the long counting period. Figures 7 and 8 show the long and short count net spectra from the deep phantom using each of the detectors. Spectra were collected using each of the wound probes and then averaged.

When the wound probes were used, regardless of long or short counting periods, the spectra did not show peaks at the higher energies and the lower energy peaks were not well resolved. Because of the small crystal size in the wound probes, some of the Compton scattered secondary photons pass through the crystal without interacting, therefore not depositing energy in the crystal and not adding to the total absorption peaks on the spectra. Some of the secondary photons may interact with the crystal by Compton scattering, but will still not result in a photopeak

because of only partial energy deposition. The result is the low-energy spectra seen in Figures 7 and 8 when using the wound probes. The spectra from the shallow and medium phantoms show peaks similar to those seen on the deep phantom spectra for all detectors.

SIGNAL-TO-NOISE RATIOS

Signal-to-noise ratios were calculated by dividing the net count rate by the background count rate for a given region of interest (ROI). Comparing the long count spectra data in each channel and visually looking at the long count spectra, ROIs were established where the signal-to-noise ratios were the greatest using each detector with each phantom These ROIs were considered the best ROI for each detector. The best ROIs for each detector were compared for the short count spectra, given a limited counting period, as would be expected in a field situation. The best ROIs varied somewhat for each detector. Figure 9 shows the signal-to-noise ratios for the long count for each detector with the shallow phantom. The signal-to-noise ratios were greater in the higher energy regions than the lower energy regions on the spectra collected by the BGO and NaI detectors.

Energy resolution of a detector is defined as the full width at half maximum (FWHM) divided by the location of the peak centroid (H_0), and is expressed as a percentage. The FWHM is the width of the distribution at a level that is half the maximum ordinate of the peak. H_o is the average peak height. The narrower the peak for a given energy region, the better the resolution and the less fluctuation recorded from pulse to pulse (Knoll, 1979). The energy resolution of the NaI detector was approximately 10% better than the BGO detector for the 63 and 93 keV peaks. This can be seen on Figures 7 and 8, where the widths of the photopeaks on the spectra collected using the NaI detector are narrower than the peaks on the spectra collected by the BGO detector. However, the BGO detector has a higher atomic number (Z = 83 for the bismuth component) than the NaI detector (Z = 11 for the sodium component), therefore the photoelectric effect is more likely to occur at higher energy with the BGO detector than the NaI detector and full energy deposition after Compton interactions are also more likely. The photofraction (ratio of the area under the

photopeak relative to the entire area under the response spectrum) of the BGO detector results in less prominent Compton continua and escape peaks (Knoll, 1979). Therefore, the area under the photopeaks in the spectra collected by the BGO detector are larger and the signal-to-noise ratios are greater than for the NaI detector as seen in Figures 7 and 8. The spectra collected using the wound probes did not show any peaks at the higher energy regions, and therefore no signal-to-noise ratios were determined for those higher regions.

EFFICIENCIES

The efficiency of each detector was calculated with the following equation:

$$\varepsilon = \frac{\textit{Net Count Rate in ROI}}{\textit{Activity}} \quad (3)$$

where: Net count rate is in counts per second and activity is in disintegrations per second

Using the long count data, the efficiencies were calculated for each detector for the best ROIs, as determined by the highest signal-to-noise regions on the spectra. These efficiencies are listed in Table 3. Using the short count data, the efficiencies calculated for each detector for the best ROIs are listed in Table 4 as well as the percent difference in the efficiencies between each detector for each phantom. In order to compare efficiencies for all detectors, a common region of interest on all the spectra for all phantoms was selected from channel 0 to 100, which encompasses the 63 to 93 keV peaks. Efficiencies were also calculated using this common ROI for each detector. The efficiencies for the best ROIs and the common ROI using the short count data are listed in Table 5. They are also graphically shown Figures 10 and 11. The short count efficiencies of all detectors for the common ROI ranged from 26% to 99% higher than the efficiencies for the best ROIs (Table 6). This is likely due to the additional counts from the additional channels included in the common ROI.

Variation in Positions Around Phantoms:

Gamma spectra were collected using each detector positioned at five additional locations around each phantom and the efficiencies were calculated. Using a ten-minute counting time and the best ROI, the efficiencies for each of the detectors for each position are listed in Table 7. Table 8 lists the efficiencies for the common ROI. For all detectors and phantoms, the highest efficiencies were obtained when the detector faces were positioned on the front or target marks on the phantoms.

Side of the Detectors:

Spectra were also collected using the side of the BGO detector, NaI detector, and one of the wound probes positioned on the shallow phantom target surface to determine whether there was a significant difference in efficiency using the face versus the side of the detectors. The same region of interest on the spectra collected using the detector face was selected for the spectra collected with the side of the detector.

For the best ROIs: Using the face of the BGO detector provided a 24% higher efficiency than when using the side of the detector with the shallow phantom. For the medium phantom, the face of the BGO detector provided a 4% higher efficiency than the side of the detector. For the deep phantom, the side provided a 7% higher efficiency than the face of the detector. The face of the NaI detector with the shallow phantom, provided a 17% higher efficiency compared to using the side of the detector. For the medium phantom, the face of the NaI detector provided a 15% higher efficiency compared to the side of the detector. For the deep phantom, the face of the NaI detector provided a 13% higher efficiency compared to the side of the detector. The side of probe 1 with the shallow phantom, provided a 50% higher efficiency than the face of the detector. For the medium phantom, using the side of the probe provided a 41% higher efficiency than the face of the detector. For the deep phantom, the side provided a 20% higher efficiency than the face.

For the common ROI: Using the face of the BGO detector provided a 20% higher efficiency than when using the side of the detector with the shallow phantom. For the medium phantom, the face of the BGO detector provided a 12% higher efficiency than the side of the

detector. For the deep phantom, the side provided the same efficiency as the face of the detector. The face of the NaI detector with the shallow phantom, provided a 15% higher efficiency compared to using the side of the detector. For the medium phantom, the face of the NaI detector provided a 13% higher efficiency compared to the side of the detector. For the deep phantom, the side of the NaI provided a 4% higher efficiency compared to the face of the detector. Probe 1 with the shallow phantom, the side of the detector provided a 48% higher efficiency than the face of the detector. For the medium phantom, using the side of the detector provided a 35% higher efficiency than the face of the detector. For the deep phantom, the side provided a 24% higher efficiency than the face. Using the side of the probe versus the face may provide higher efficiencies because the side of the crystal in the probe is 0.5 inches wide, providing more area for gamma interactions than the face, which is 0.125 inches in diameter. Tables 9 and 10 summarize the efficiencies for the best ROIs and the common ROI using the faces versus the sides of the detectors.

LOWER LIMIT OF DETECTION (LLD)

The lower limit of detection can be described as the lowest amount of net radioactivity that can be measured by a detection system. The LLD depends on the background counting rate of the detector, the detector size, the geometry of the source, the geometry of the detector with respect to the source, the counting period, the energy of the gamma radiation and its frequency of emission (Toohey, 1991). Based on the activities and relative efficiencies determined for each detector, LLDs were calculated using the same ROIs established from the long count data for each detector and for the common ROI (channel zero to 100), using each of the phantoms. The LLDs with 95% confidence were calculated using the following equation (Altshuler et al, 1963):

$$LLD = \frac{4.66 \; x \; (STD \;\; DEV \;\; of \;\; Bkd)}{\varepsilon} \qquad (4)$$

where: ε is the efficiency of the detector in counts per disintegration

STD DEV is the standard deviation of the background count rate for a particular ROI in counts per second

For the shallow phantom (best ROI), the lowest LLD was 0.256 μCi for the BGO and NaI detectors. For the medium and deep phantoms (best ROI), the lowest LLDs were 1.24 μCi and 4.58 μCi, respectively, for the BGO detector. For the common ROI, the lowest LLD was 0.156 μCi for the BGO detector with the shallow phantom. For the medium phantom, the lowest LLD was 0.092 μCi for the NaI detector. For the deep phantom, the lowest LLD was 0.276 μCi for the BGO detector. Tables 11 and 12 summarize all the LLDs for the best and common ROIs (short count).

SINGLE CHANNEL ANALYZER (SCALER) DATA

The plotted data collected at 0.02 V increments from the shallow and blank phantoms using each of the detectors connected to the scaler showed rough peaks at the lower channel numbers which correlate to the lower energy regions on the spectra displayed using an MCA. There were a limited number of channels in which to collect the data and therefore a limited number of data points to display a spectra. The plotted spectra and the corresponding signal-to-noise ratios for the BGO detector, NaI detector and wound probe 2 are shown in Figure 12. The signal-to-noise ratios are somewhat crude and unsmoothed just as the plotted spectra, but do indicate that the signal from the source radiation is higher than the signal from the background radiation in the lower channel regions.

Net Count Rates and Efficiencies:

The net counts in ten minutes for each detector attached to the scaler were collected at

the same six positions around the phantoms. Each detector was set at its operating voltage and a lower threshold of 0.02 volt was set on the scaler, with no upper threshold. The relative efficiencies for the entire spectra were calculated using the net count rates and are listed in Table 13. The efficiencies for the target position was highest compared to the other five positions around the phantom surface. The efficiencies calculated from the scaler data are of the same orders of magnitude as the efficiencies calculated using the MCA short count data for the common ROI listed in Table 7.

SOURCES OF ERROR AND ERROR ANALYSIS

The errors in this experiment were from the random nature of radioactive decay of the depleted uranium, the interaction of radiation with matter, and the various random events in the photomultiplier tube (pmt). The random events in the pmt include the number of electrons excited, the number of photons reaching the pmt, the number of photoelectrons produced, and the number of secondary electrons produced at each dynode. Other errors include source counting, errors in the calculated activities of the sources, the efficiencies, and the lower limits of detection. These reported errors were quantified by error propagation.

The method in which the background was determined and subtracted from the source spectra has some error associated with it. Although background spectra were subtracted, the photopeaks were not isolated from the Compton continua on the spectra which makes it more difficult to define a precise ROI.

Another source of error was in background counts. There are several contributors of background. First, there was no shielding around the detector to block out surrounding gammas from within the room. The detector material and the material of the phantom can also contribute to background (Toohey, 1991).

CONCLUSIONS AND RECOMMENDATIONS

The first objective of this research was to describe the calibration protocols using depleted uranium in three wound phantoms. Sealed gamma sources were used to energy calibrate the detectors that were connected to an MCA. Long count gamma spectra were then collected from each phantom using each detector. Background spectra were collected from the blank phantom and subtracted from the source spectra. From these net spectra, the best ROIs for each detector were selected using the long count data. Using the same ROIs, relative efficiencies and lower limits of detection were calculated for the short count (ten minutes) data.

Short count spectra were collected at varying positions around the phantoms using each detector. Short count spectra were also collected using the sides of the BGO detector, the NaI detector, and one of the wound probes.

The second objective of this research was to compare the relative efficiencies of three types of scintillation detectors for detection of depleted uranium in wounds as a function of angle and depth. Since the geometry of each source was not well-defined, the relative efficiencies of the detectors were determined rather than their absolute efficiencies.

The best ROI (highest signal-to-noise ratio) for the BGO detector was determined to be from about 49.3 to 106.9 keV for the shallow phantom and from approximately 995 to 1010 keV for the medium and deep phantoms. For the NaI detector, the best ROI was from about 48.6 to 105.9 keV for the shallow phantom and from approximately 1001 to 1017 keV for the medium and deep phantoms. For the wound probes averaged, the best ROI for the shallow phantom was from 48.2 to 107.0 keV and from about 50.4 to 106.6 keV for the medium and deep phantoms.

For the shallow phantom, best ROI, the BGO detector had a 11% higher efficiency than the NaI detector and a 98.9% higher efficiency than the averaged wound probes. For the medium phantom, best ROI, the BGO had a 48% higher efficiency than the NaI and an 64% higher

efficiency than the averaged probes. For the deep phantom, best ROI, the BGO detector had a 54% higher efficiency than the NaI and an 57% higher efficiency than the averaged probes.

For the shallow phantom, common ROI, the BGO detector had an 11% higher efficiency than the NaI and a 98% higher efficiency than the wound probes. For the medium phantom, the BGO had a 6% higher efficiency than the NaI and 99% higher efficiency than the averaged wound probes. The BGO also had a 14% higher efficiency than the NaI and a 99% higher efficiency than the wound probes for the deep phantom. The lowest LLDs for the best and common ROIs corresponded to the detectors with the highest efficiencies for the particular region and phantom.

Changing the location of the detector face to different positions around the phantoms showed a difference in efficiency for each of the detectors. Since the geometry and size of the source within each phantom varied, and each source is not suspended in the middle of the phantoms (as indicated in the x-rays of the phantoms), it was expected and shown that the efficiencies varied as the detectors were placed around each location. The highest efficiency was seen for all detectors when the detector faces were placed on the front of the phantoms where the target marks are located. For the best and common ROIs, the detector with the highest efficiency was the BGO detector for all positions on the medium and deep phantoms except the back position around the medium phantom. The back position (common ROI) where the efficiency of the BGO detector was not the highest was only 5% less than the efficiency of the NaI. For the best and common ROIs, the NaI detector had the highest efficiencies for more of the positions around the shallow phantom than the BGO detector and wound probes.

The scaler used in this experiment was only capable of recording the counts or count rates from the DU sources. It was not capable of outputting a gamma spectra. However, using the information from the gamma spectra collected from the MCA, information regarding the data collected from the scaler can be inferred. The scaler has a range of window settings from 0.01 to 1 volt. Using a window of 0.02 volts, a spectra was created using the data from each incremental increase in the window setting. The spectra manually plotted from the scaler was somewhat similar in shape to the spectra from the MCA for the lower energy region but are not well-defined.

Similar to the method used to determine a region of interest from the gamma spectra, the region of interest on the manually plotted spectra was determined to be where the signal-to-noise ratio was the greatest. This region, in turn, was used for determining an efficiency for the detectors connected to the scaler. The capabilities of the detectors connected to the scaler were examined because the scaler is portable, which was one of the criteria the Army wanted in a detection system capable of detecting DU in wounds. Whereas the efficiencies of the BGO detector, NaI detector, and wound probes varied, all are equally easy to use and are portable.

Studies comparing sodium iodide detectors with solid state detectors such as the high purity germanium (HPGe) detectors have shown that the Ge detector can give a better resolution when measuring low-energy photons, while maintaining a comparable efficiency (King, 1977). The higher resolution of the HPGe provides a better signal-to-noise ratio between the total absorption peaks from the low-energy photons and background (Palmer, 1984). The regions where there are better signal-to-noise ratios are more easily identified and therefore a more accurate determination of efficiency can be made for those energy regions. Although high purity germanium detectors have higher energy resolutions than sodium iodide and BGO detectors, the HPGe does not meet the requirement for portability because it must be housed within a vacuum-tight container, where low temperatures are maintained by a reservoir of liquid nitrogen to prevent thermally induced leakage of the current during operation.

A 3x3x2 mm^3 spectrometer grade cadmium-zinc-tellurium (Cd-Zn-Te) detector made by eV Products, has been demonstrated to detect low-energy photons from americium-241 (eV Products, 1997). Initial measurements using this detector with the DU phantoms indicated extremely low detection efficiency potential. However, further measurements using this detector may be required to verify the efficiency of detecting the low-energy photons from depleted uranium. Other detectors such as phoswich detectors may also have potential for low-gamma detection.

The third objective was to provide the data from the detectors and recommendations to the Army Radiation Research Office regarding the relative efficiencies of the detectors. From the data collected in this research, these recommendations are:

1. Of the three types of detectors, the BGO detector has the highest efficiency for all depths of DU sources when looking at the best ROIs. For the shallow depth source, the BGO has an efficiency of 7.4×10^{-4} and an LLD of 0.26 μCi. For the medium depth source, the BGO has an efficiency of 2.5×10^{-5} and an LLD of 1.24 μCi. For the deep phantom, the BGO has an efficiency of 6.9×10^{-6} and an LLD of 4.58 μCi. The BGO detector also has the highest efficiency when looking at the common ROI for all depth of DU sources. For the shallow phantom, the BGO detector has an efficiency of 1.0×10^{-3} and an LLD of 0.156 μCi. For the medium phantom, the BGO has an efficiency of 1.7×10^{-3} and an LLD of 0.094 μCi. For the deep phantom, the BGO has an efficiency of 5.8×10^{-4} and an LLD of 0.276 μCi. The efficiencies using the common ROI were higher than the efficiencies using the best ROIs for each detector with each phantom, therefore using the common ROI is recommended.

2. In all measurements for efficiency with the BGO and NaI detectors, using the face of the detectors provided higher efficiencies than using the sides of the detectors except for two measurements. The two measurements where using the side provided higher efficiencies were only 4% and 7% higher than when using the face of the detectors. Therefore, using the faces of the BGO and NaI detectors is recommended when counting DU sources. Using the sides of the probes against the phantom surfaces, however, provided at least a 20% higher efficiency than when using the faces of the probes for all phantoms.

3. In a field situation, a detector connected to the scaler can provide a quick and portable way of screening for DU radiation suspected in a wound. Although the scaler can only provide counts and count rates, it can provide enough information for the technician to conduct a quick assessment of DU-suspected wounds. A more detailed assessment of the patient can then be done in a hospital environment with the detector connected to an MCA, where a gamma spectra of the DU-suspected wound could be examined to see if the fragment displays characteristics of depleted uranium. Portable MCAs are available in the market, but use of one may require more training and more time which may not be feasible in a battlefield situation. The detector connected to the scaler should be checked against a standard source of depleted uranium or a source with

similar gamma energies as depleted uranium prior to use in the field. The lower threshold setting (Chn 1 on scaler) should be set at about 0.02 volts to discriminate against electronic noise and the high voltage should be set at about 900 to 1000 volts. A background count should first be taken and with the same lower threshold and operating voltage settings, a DU-suspected wound should be counted for the same counting period (approximately 5 to 10 minutes) as the background. If the number of counts from the wound is about two to three times above background, then it may contain depleted uranium and the wound should then be further evaluated using an MCA to look at the gamma spectra.

4. In this study, a limited number of measurements were taken to determine the efficiencies of the detectors. Therefore, it is recommended that further measurements of efficiencies be taken to verify the results from this study. Extreme temperatures that may be encountered in a battlefield situation may affect the response of the detectors, therefore the detectors' responses should be checked in temperatures similar to those expected in the situations where the detectors will be used.

5. Another consideration when counting in the field is to shield the detector against background radiations by using some type of lead shielding around the detector.

6. In this research, net spectra were determined by subtracting background spectra collected using a blank phantom from a source spectra collected from a DU-imbedded phantom. Other methods to subtract the background spectra from the source spectra could be examined to allow a better determination of the counts under the photopeaks in the regions of interest. There are spectra stripping techniques (Spitz et al, 1985) and software programs that subtract background spectra and Compton scattering events from the photopeaks in gamma spectroscopy that could allow for more precise calculation of the efficiencies of the detectors for a particular energy region.

REFERENCES

Altshuler, B. and Pasternak, B. Statistical measures of the lower limit of detection of a radioactivity counter. Health Phys. 9:293-298; 1963.

Armed Forces Radiobiology Research Institute (AFRRI). Assessment of the risks from imbedded fragments of depleted uranium. Bethesda: Technical Report 93-1; 1993.

Armed Forces Radiobiology Research Institute (AFRRI). Protocol for monitoring gulf war veterans with imbedded fragments of depleted uranium. Bethesda: Technical Report 93-2; 1993.

Army Environmental Policy Institute (AEPI). Health and environmental consequences of depleted uranium use by the U.S. Army. Atlanta: Summary Report to Congress; 1994.

Army Environmental Policy Institute (AEPI). Health and environmental consequences of depleted uranium use in the U.S. Army. Atlanta: Technical Report; 1995.

Bureau of Radiological Health, U.S. Department of Health, Education, and Welfare, Public Health Service. Radiological health handbook: revised edition - January 1970. Rockville: 1970: pp. 120.

eV Products. Specifications data sheets. Saxonburg, PA; 1997.

International Commission on Radiological Protection (ICRP). Radionuclide Transformations - Energy and Intensity of Emissions. Oxford: ICRP Publication 38; 1983.

King, A.; Scott, L. M.; Disney, J. L. Comparison of sodium iodide and solid state detectors for the measurement of lung-stored uranium. Health Phys. 34: 112-115; 1977.

Knoll, G. F. Radiation detection and measurement. 2nd ed. New York: John Wiley and Sons, Inc. 1979: pp. 234, 306-307, 322-323.

Olsen, P. C. Depleted uranium wound calibration phantom for United States Army TMDE activity. Battelle, Pacific Northwest Laboratory, Washington: Contract #PNL21603; 1994.

Palmer, H. E. and Rieksts, G. A. The use of planar high-purity Ge detectors for in vivo measurement of low-energy photon emitters. Health Phys. 47: 569, 577-578; 1984.

Spitz, H. B.; Buschbom, R. L., Rieksts, G. A., and Palmer, H. E. A new method for analyzing high-resolution spectra from whole-body counter in-vivo measurements. Health Phys. 49: 1085-1096; 1985.

Toohey, R. et al. Current status of whole-body counting as a means to detect and quantify previous exposures to radioactive materials. Health Phys. 60 (Sup. 1): 7-42; 1991.

TABLES

Table 1. Gamma radiations from ^{238}U, ^{234}Th, and ^{234m}Pa and frequencies of emission (ICRP 38, 1983)

Radionuclide	Energy (keV)	Frequency of Emission $(Bq\text{-}s)^{-1}$
^{238}U	49.55	6.97×10^{-4}
^{234}Th	62.86	1.77×10^{-4}
	63.29	3.81×10^{-2}
	83.30	7.04×10^{-4}
	92.38	2.73×10^{-2}
	92.80	2.69×10^{-2}
	112.8	2.42×10^{-3}
^{234m}Pa	766.6	2.07×10^{-3}
	1001.0	5.89×10^{-3}

Table 2. Description of phantom heights, depths of DU, masses of DU, and activities.

Phantom	Height (cm)	DU Depth (cm)	DU Mass (g)	Activity (μCi)
Shallow	20.3	0.97	8.69 +/- 0.01	2.9 +/- 0.003
Medium	18.5	3.91	21.30 +/- 0.01	7.1 +/- 0.003
Deep	20.0	7.73	36.38 +/- 0.01	12.0 +/- 0.003
Blank	20.8	none	none	none

Table 3. Best regions of interest (ROIs) for each detector and efficiencies (detector face on target surface - long count)

Shallow Phantom

Detector	best ROI Energy (keV)	Efficiency (ε)	$\delta\ \varepsilon$
BGO	48.7 to 106.3	7.3×10^{-4}	1.0×10^{-6}
NaI	48.5 to 106.6	7.2×10^{-4}	1.0×10^{-6}
Wound Probes Averaged	48.4 to 107.6	9.4×10^{-6}	5.3×10^{-8}

Medium Phantom

Detector	best ROI Energy (keV)	Efficiency (ε)	$\delta\ \varepsilon$
BGO	993.1 to 1007.6	2.8×10^{-5}	6.9×10^{-8}
NaI	1036.2 to 1052.6	1.3×10^{-5}	3.3×10^{-8}
Wound Probes Averaged	48.4 to 107.6	8.1×10^{-6}	2.6×10^{-8}

Deep Phantom

Detector	best ROI Energy (keV)	Efficiency (ε)	$\delta\ \varepsilon$
BGO	998.3 to 1012.9	7.2×10^{-6}	2.0×10^{-8}
NaI	1000.5 to 1016.9	3.4×10^{-6}	1.4×10^{-8}
Wound Probes Averaged	47.7 to 106.1	2.5×10^{-6}	1.3×10^{-8}

Table 4. Efficiencies and percent differences in efficiencies between each detector for each phantom (best ROIs)

Shallow Phantom

BGO	NaI	% Difference in Efficiency
* 7.4×10^{-4}	6.6×10^{-4}	11
BGO	Wound Probes	% Difference in Efficiency
* 7.4×10^{-4}	8.3×10^{-6}	98.9
NaI	Wound Probes	% Difference in Efficiency
* 6.6×10^{-4}	8.3×10^{-6}	98.7

Medium Phantom

BGO	NaI	% Difference in Efficiency
* 2.5×10^{-5}	1.3×10^{-5}	48
BGO	Wound Probes	% Difference in Efficiency
* 2.5×10^{-5}	8.9×10^{-6}	64
NaI	Wound Probes	% Difference in Efficiency
* 1.3×10^{-5}	8.9×10^{-6}	32

Deep Phantom

BGO	NaI	% Difference in Efficiency
* 6.9×10^{-6}	3.2×10^{-6}	54
BGO	Wound Probes	% Difference in Efficiency
* 6.9×10^{-6}	3.0×10^{-6}	57
NaI	Wound Probes	% Difference in Efficiency
* 3.2×10^{-6}	3.0×10^{-6}	6

* denotes higher efficiency

Table 5. Best and common regions of interest (ROIs) for each detector and efficiencies (detector face on target surface - short count)

Shallow Phantom

Detector	Best ROI Energy (keV)	Efficiency (ε)	$\delta\varepsilon$	Common ROI (Chn 0 - 100)	
				Efficiency (ε)	$\delta\varepsilon$
BGO	49.3 to 106.9	7.4×10^{-4}	6.2×10^{-6}	1.0×10^{-3}	8.0×10^{-6}
NaI	48.6 to 105.9	6.6×10^{-4}	5.8×10^{-6}	8.9×10^{-4}	7.3×10^{-6}
Wound Probes Averaged	48.2 to 107.0	8.3×10^{-6}	5.2×10^{-7}	1.6×10^{-5}	7.7×10^{-7}

Medium Phantom

Detector	Best ROI Energy (keV)	Efficiency (ε)	$\delta\varepsilon$	Common ROI (Chn 0 -100)	
				Efficiency (ε)	$\delta\varepsilon$
BGO	1000.2 to 1014.7	2.5×10^{-5}	4.4×10^{-7}	1.7×10^{-3}	4.4×10^{-6}
NaI	996.0 to 1011.8	1.3×10^{-5}	3.2×10^{-7}	1.6×10^{-3}	4.1×10^{-6}
Wound Probes Averaged	50.4 to 106.6	8.9×10^{-6}	2.8×10^{-7}	1.7×10^{-5}	4.0×10^{-7}

Deep Phantom

Detector	Best ROI Energy (keV)	Efficiency (ε)	$\delta\varepsilon$	Common ROI (Chn 0 -100)	
				Efficiency (ε)	$\delta\varepsilon$
BGO	992.9 to 1007.4	6.9×10^{-6}	1.9×10^{-7}	5.8×10^{-4}	2.2×10^{-6}
NaI	1007.1 to 1022.8	3.2×10^{-6}	1.3×10^{-7}	5.0×10^{-4}	2.0×10^{-6}
Wound Probes Averaged	50.4 to 106.6	3.0×10^{-6}	1.3×10^{-7}	5.0×10^{-6}	2.0×10^{-7}

Table 6. Comparison of efficiencies between best ROI and common ROI for each detector with each phantom

Shallow Phantom

Detector	Efficiency (Best ROI)	Efficiency (Common ROI)	% Difference
BGO	7.4×10^{-4}	* 1.0×10^{-3}	26
NaI	6.6×10^{-4}	* 8.9×10^{-4}	26
Wound Probes Averaged	8.3×10^{-6}	* 1.6×10^{-5}	48

Medium Phantom

Detector	Efficiency (Best ROI)	Efficiency (Common ROI)	% Difference
BGO	2.5×10^{-5}	* 1.7×10^{-3}	98
NaI	1.3×10^{-5}	* 1.6×10^{-3}	99
Wound Probes Averaged	8.9×10^{-6}	* 1.7×10^{-5}	48

Deep Phantom

Detector	Efficiency (Best ROI)	Efficiency (Common ROI)	% Difference
BGO	6.9×10^{-6}	* 5.8×10^{-4}	99
NaI	3.2×10^{-6}	* 5.0×10^{-4}	99
Wound Probes Averaged	3.0×10^{-6}	* 5.0×10^{-6}	40

* denotes the higher efficiency between the best and common ROIs

Table 7. Relative efficiencies of detectors at varying positions around the phantom surface for the best ROIs (short count)

Shallow Phantom

Position on Phantom	BGO		NaI		Wound Probes Averaged	
	ε	$\delta\,\varepsilon$	ε	$\delta\,\varepsilon$	ε	$\delta\,\varepsilon$
Front	7.4×10^{-4}	6.2×10^{-6}	6.6×10^{-4}	5.8×10^{-6}	8.3×10^{-6}	5.2×10^{-7}
Back	2.8×10^{-6}	5.2×10^{-6}	5.7×10^{-5}	4.7×10^{-6}	3.5×10^{-7}	4.0×10^{-7}
Left	7.5×10^{-5}	5.2×10^{-6}	1.3×10^{-4}	4.8×10^{-6}	1.1×10^{-6}	4.0×10^{-7}
Right	6.0×10^{-5}	5.2×10^{-6}	1.2×10^{-4}	4.7×10^{-6}	9.9×10^{-7}	4.0×10^{-7}
Top	2.1×10^{-5}	4.9×10^{-6}	2.2×10^{-5}	4.5×10^{-6}	2.2×10^{-7}	3.6×10^{-7}
Bottom	1.0×10^{-5}	4.9×10^{-6}	6.1×10^{-6}	4.4×10^{-6}	1.3×10^{-7}	3.6×10^{-7}

Medium Phantom

Position on Phantom	BGO		NaI		Wound Probes Averaged	
	ε	$\delta\,\varepsilon$	ε	$\delta\,\varepsilon$	ε	$\delta\,\varepsilon$
Front	2.5×10^{-5}	4.4×10^{-7}	1.3×10^{-5}	3.2×10^{-7}	8.9×10^{-6}	2.8×10^{-7}
Back	1.6×10^{-6}	2.2×10^{-7}	9.5×10^{-7}	1.7×10^{-7}	4.5×10^{-7}	1.6×10^{-7}
Left	6.2×10^{-6}	2.6×10^{-7}	2.3×10^{-6}	1.9×10^{-7}	1.4×10^{-6}	1.8×10^{-7}
Right	8.4×10^{-6}	2.9×10^{-7}	3.4×10^{-6}	2.1×10^{-7}	2.2×10^{-6}	2.0×10^{-7}
Top	1.1×10^{-5}	3.1×10^{-7}	4.4×10^{-6}	2.3×10^{-7}	2.4×10^{-6}	1.9×10^{-7}
Bottom	2.2×10^{-6}	2.3×10^{-7}	1.1×10^{-6}	1.7×10^{-7}	8.3×10^{-7}	1.6×10^{-7}

Deep Phantom

Position on Phantom	BGO		NaI		Wound Probes Averaged	
	ε	$\delta\,\varepsilon$	ε	$\delta\,\varepsilon$	ε	$\delta\,\varepsilon$
Front	6.9×10^{-6}	1.9×10^{-7}	3.2×10^{-6}	1.3×10^{-7}	3.0×10^{-6}	1.3×10^{-7}
Back	3.8×10^{-6}	1.6×10^{-7}	1.8×10^{-6}	1.2×10^{-7}	1.2×10^{-6}	1.1×10^{-7}
Left	6.1×10^{-6}	1.8×10^{-7}	2.9×10^{-6}	1.4×10^{-7}	1.7×10^{-6}	1.2×10^{-7}
Right	4.5×10^{-6}	1.6×10^{-7}	2.0×10^{-6}	1.2×10^{-7}	1.4×10^{-6}	1.2×10^{-7}
Top	4.4×10^{-6}	1.7×10^{-7}	1.9×10^{-6}	1.2×10^{-7}	1.3×10^{-6}	1.1×10^{-7}
Bottom	4.4×10^{-6}	1.7×10^{-7}	2.0×10^{-6}	1.2×10^{-7}	1.4×10^{-6}	1.1×10^{-7}

Note: ε = Efficiency

Table 8. Relative efficiencies of detectors at varying positions around the phantom surface for the common ROI (short count)

Shallow Phantom

Position on Phantom	BGO		NaI		Wound Probes Averaged	
	ε	$\delta\varepsilon$	ε	$\delta\varepsilon$	ε	$\delta\varepsilon$
Front	1.0×10^{-3}	8.1×10^{-6}	8.9×10^{-4}	7.3×10^{-6}	1.6×10^{-5}	7.7×10^{-7}
Back	9.7×10^{-5}	7.2×10^{-6}	9.2×10^{-5}	6.2×10^{-6}	1.4×10^{-7}	6.0×10^{-7}
Left	9.1×10^{-5}	7.1×10^{-6}	1.8×10^{-4}	6.2×10^{-6}	1.7×10^{-6}	6.1×10^{-7}
Right	9.8×10^{-5}	7.1×10^{-6}	1.7×10^{-4}	6.2×10^{-6}	2.3×10^{-6}	6.2×10^{-7}
Top	2.9×10^{-5}	6.8×10^{-6}	3.1×10^{-5}	5.9×10^{-6}	9.2×10^{-7}	5.4×10^{-7}
Bottom	2.4×10^{-5}	6.8×10^{-6}	1.0×10^{-5}	5.9×10^{-6}	1.7×10^{-7}	5.5×10^{-7}

Medium Phantom

Position on Phantom	BGO		NaI		Wound Probes Averaged	
	ε	$\delta\varepsilon$	ε	$\delta\varepsilon$	ε	$\delta\varepsilon$
Front	1.7×10^{-3}	4.4×10^{-6}	1.6×10^{-3}	4.1×10^{-6}	1.7×10^{-5}	4.0×10^{-7}
Back	1.8×10^{-4}	3.0×10^{-6}	1.9×10^{-4}	2.7×10^{-6}	1.3×10^{-6}	2.6×10^{-7}
Left	4.1×10^{-4}	3.3×10^{-6}	3.9×10^{-4}	2.9×10^{-6}	3.6×10^{-6}	2.8×10^{-7}
Right	5.8×10^{-4}	3.4×10^{-6}	4.9×10^{-4}	3.0×10^{-6}	5.5×10^{-6}	3.0×10^{-7}
Top	7.2×10^{-4}	3.5×10^{-6}	6.9×10^{-4}	3.2×10^{-6}	6.4×10^{-6}	3.0×10^{-7}
Bottom	2.1×10^{-4}	3.0×10^{-6}	2.1×10^{-4}	2.7×10^{-6}	1.9×10^{-6}	2.5×10^{-7}

Deep Phantom

Position on Phantom	BGO		NaI		Wound Probes Averaged	
	ε	$\delta\varepsilon$	ε	$\delta\varepsilon$	ε	$\delta\varepsilon$
Front	5.8×10^{-4}	2.2×10^{-6}	5.0×10^{-4}	2.0×10^{-6}	5.0×10^{-6}	2.0×10^{-7}
Back	3.8×10^{-4}	2.1×10^{-6}	3.7×10^{-4}	1.9×10^{-6}	3.0×10^{-6}	1.8×10^{-7}
Left	5.4×10^{-4}	2.2×10^{-6}	5.0×10^{-4}	2.0×10^{-6}	4.1×10^{-6}	1.9×10^{-7}
Right	4.2×10^{-4}	2.1×10^{-6}	3.9×10^{-4}	1.9×10^{-6}	3.3×10^{-6}	1.8×10^{-7}
Top	3.7×10^{-4}	2.0×10^{-6}	3.3×10^{-4}	1.8×10^{-6}	3.2×10^{-6}	1.7×10^{-7}
Bottom	3.9×10^{-4}	2.0×10^{-6}	3.5×10^{-4}	1.8×10^{-6}	3.3×10^{-6}	1.7×10^{-7}

Note: ε = Efficiency

Table 9. Efficiencies for best ROIs using face versus side of detectors positioned on target surface (short count)

Shallow Phantom

Detector	Face		Side		% Difference in
	ε	δ ε	ε	δ ε	ε
BGO	* 7.4×10^{-4}	6.2×10^{-6}	5.6×10^{-4}	5.8×10^{-6}	24
NaI	* 6.6×10^{-4}	5.8×10^{-6}	5.5×10^{-4}	5.5×10^{-6}	17
Wound Probe 1	9.0×10^{-6}	5.7×10^{-7}	* 1.8×10^{-5}	6.9×10^{-7}	50

Medium Phantom

Detector	Face		Side		% Difference in
	ε	δ ε	ε	δ ε	ε
BGO	* 2.5×10^{-5}	4.4×10^{-7}	2.4×10^{-5}	4.3×10^{-7}	4
NaI	* 1.3×10^{-5}	3.2×10^{-7}	1.1×10^{-5}	2.9×10^{-7}	15
Wound Probe 1	1.0×10^{-5}	2.7×10^{-7}	* 1.7×10^{-5}	3.8×10^{-7}	41

Deep Phantom

Detector	Face		Side		% Difference in
	ε	δ ε	ε	δ ε	ε
BGO	6.9×10^{-6}	1.9×10^{-7}	* 7.4×10^{-6}	2.0×10^{-7}	7
NaI	* 3.2×10^{-6}	1.3×10^{-7}	2.8×10^{-6}	1.3×10^{-7}	13
Wound Probe 1	3.3×10^{-6}	1.2×10^{-7}	* 4.1×10^{-6}	1.7×10^{-7}	20

Note: ε = Efficiency

* denotes the higher efficiency between the face and side of the detector

Table 10. Efficiencies for common ROI using face versus side of detectors positioned on target surface (short count)

Shallow Phantom

Detector	Face		Side		% Difference in
	ε	δ ε	ε	δ ε	ε
BGO	* 1.0×10^{-3}	8.0×10^{-6}	8.0×10^{-4}	8.0×10^{-6}	20
NaI	* 8.9×10^{-4}	7.3×10^{-6}	7.6×10^{-4}	7.1×10^{-6}	15
Wound Probe 1	1.3×10^{-5}	7.2×10^{-7}	* 2.5×10^{-5}	8.5×10^{-7}	48

Medium Phantom

Detector	Face		Side		% Difference in
	ε	δ ε	ε	δ ε	ε
BGO	* 1.7×10^{-3}	4.4×10^{-6}	1.5×10^{-3}	4.3×10^{-6}	12
NaI	* 1.6×10^{-3}	4.1×10^{-6}	1.4×10^{-3}	4.0×10^{-6}	13
Wound Probe 1	1.7×10^{-5}	4.0×10^{-7}	* 2.6×10^{-5}	4.7×10^{-7}	35

Deep Phantom

Detector	Face		Side		% Difference in
	ε	δ ε	ε	δ ε	ε
BGO	5.8×10^{-4}	2.2×10^{-6}	5.8×10^{-4}	2.3×10^{-6}	0
NaI	5.0×10^{-4}	2.0×10^{-6}	* 5.2×10^{-4}	2.1×10^{-6}	4
Wound Probe 1	5.0×10^{-6}	2.0×10^{-7}	* 6.6×10^{-6}	2.1×10^{-7}	24

Note: ε = Efficiency

* denotes the higher efficiency between the face and side of the detector

Table 11. LLDs of each detector for best ROIs (detector face on target surface - short count)

DETECTORS	PHANTOMS					
	SHALLOW		MEDIUM		DEEP	
	LLD (μCi)	δ LLD (μCi)	LLD (μCi)	δ LLD (μCi)	LLD (μCi)	δ LLD (μCi)
BGO	0.256	0.002	1.24	0.02	4.58	0.13
NaI	0.256	0.002	1.84	0.05	7.2	0.3
Wound Probes Averaged	2.04	0.13	1.99	0.06	5.9	0.3

Table 12. LLDs of detectors for common ROI (detector face positioned on target surface - short count)

DETECTORS	PHANTOMS					
	SHALLOW		MEDIUM		DEEP	
	LLD (μCi)	δ LLD (μCi)	LLD (μCi)	δ LLD (μCi)	LLD (μCi)	δ LLD (μCi)
BGO	0.156	0.0012	0.094	0.0002	0.276	0.0011
NaI	0.161	0.0013	0.092	0.0002	0.285	0.0011
Wound Probes Averaged	0.85	0.04	0.82	0.02	2.598	0.099

Table 13. Efficiencies for shallow, medium, and deep phantoms using scaler data (short count - lower threshold set at 0.02 volts)

Shallow

Position on Phantom	BGO		NaI		Probe 1	
	Efficiency	δ	Efficiency	δ	Efficiency	δ
Front	1.2E-04	5.0E-06	1.3E-03	1.0E-05	1.5E-05	7.3E-07
Back	-5.4E-06	4.7E-06	-1.1E-05	9.1E-06	9.5E-07	5.7E-07
Left	-1.3E-05	4.8E-06	2.9E-05	9.1E-06	1.6E-06	6.0E-07
Right	1.9E-05	4.8E-06	-1.1E-05	9.1E-06	2.1E-06	6.0E-07
Top	-1.0E-05	4.9E-06	2.5E-05	9.1E-06	-4.2E-07	5.8E-07
Bottom	2.6E-05	4.8E-06	3.1E-05	9.1E-06	-1.7E-07	5.6E-07

Medium

Position on Phantom	BGO		NaI		Probe 1	
	Efficiency	δ	Efficiency	δ	Efficiency	δ
Front	9.2E-04	3.1E-06	3.2E-03	6.0E-06	1.5E-05	3.9E-07
Back	8.1E-05	2.1E-06	3.6E-04	4.0E-06	1.6E-06	2.5E-07
Left	2.0E-04	2.3E-06	6.3E-04	4.2E-06	4.1E-06	2.8E-07
Right	2.8E-04	2.4E-06	7.0E-04	4.3E-06	5.3E-06	2.9E-07
Top	3.5E-04	2.5E-06	1.1E-03	4.6E-06	5.1E-06	3.0E-07
Bottom	1.0E-04	2.1E-06	3.3E-04	4.0E-06	1.7E-06	2.5E-07

Deep

Position on Phantom	BGO		NaI		Probe 1	
	Efficiency	δ	Efficiency	δ	Efficiency	δ
Front	2.7E-04	1.5E-06	1.0E-03	3.0E-06	4.9E-06	1.9E-07
Back	1.8E-04	1.4E-06	7.0E-04	2.7E-06	3.2E-06	1.7E-07
Left	2.4E-04	1.5E-06	9.2E-04	2.9E-06	4.1E-06	1.8E-07
Right	1.8E-04	1.4E-06	7.3E-04	2.8E-06	3.3E-06	1.7E-07
Top	1.4E-04	1.4E-06	6.2E-04	2.7E-06	2.8E-06	1.7E-07
Bottom	1.6E-04	1.4E-06	6.3E-04	2.7E-06	3.0E-06	1.7E-07

FIGURES

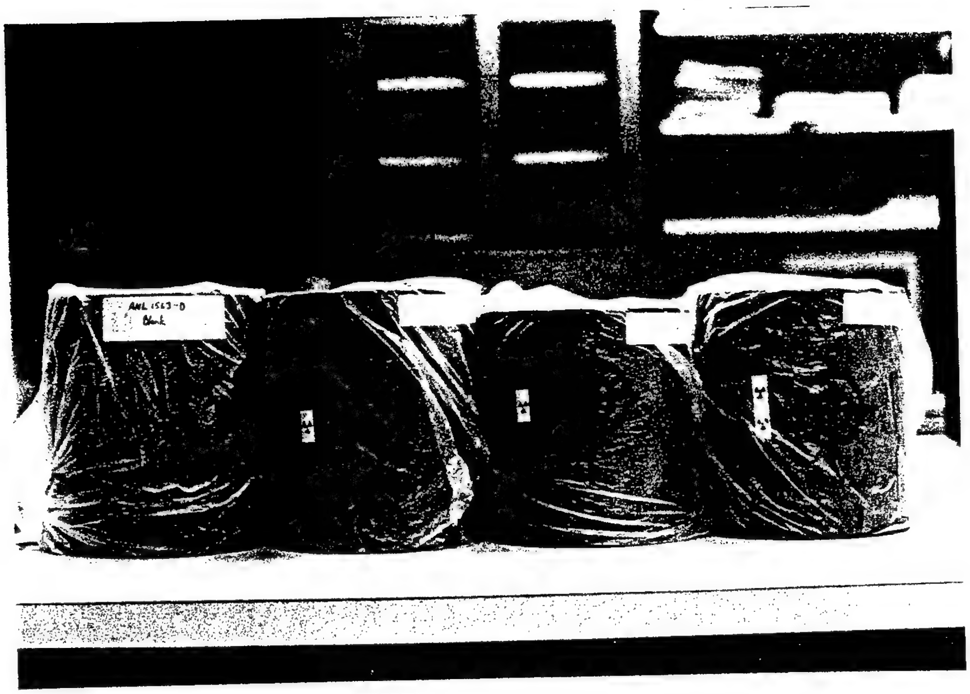

Figure 1. Tissue-equivalent wound phantoms

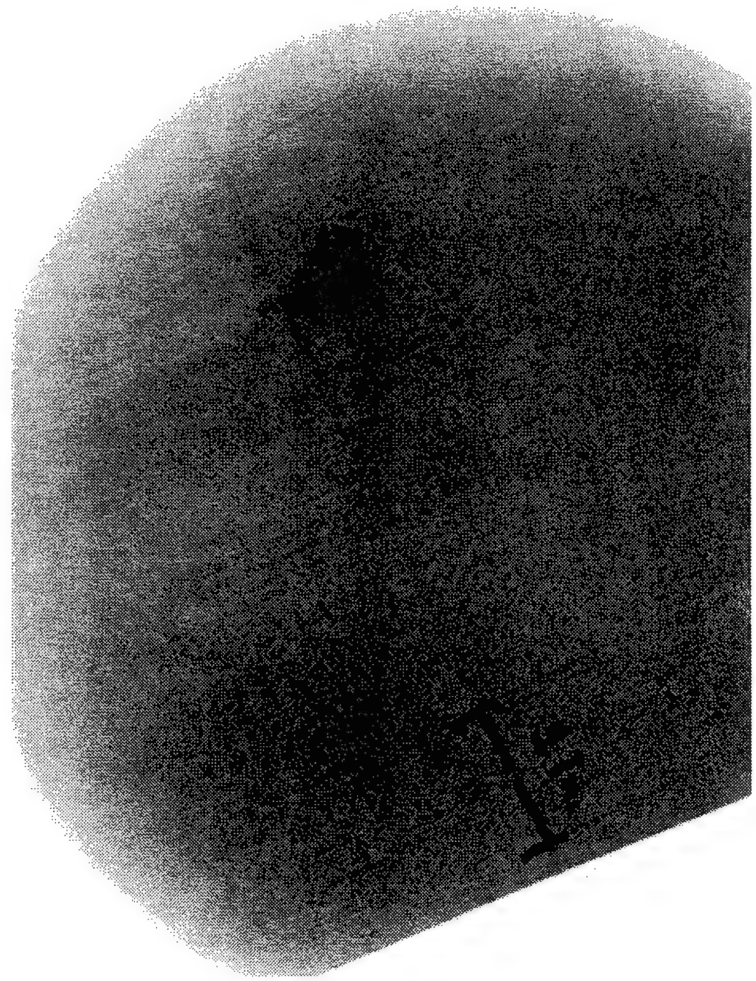

Figure 2. X-ray of DU fragment from the top view of the medium phantom

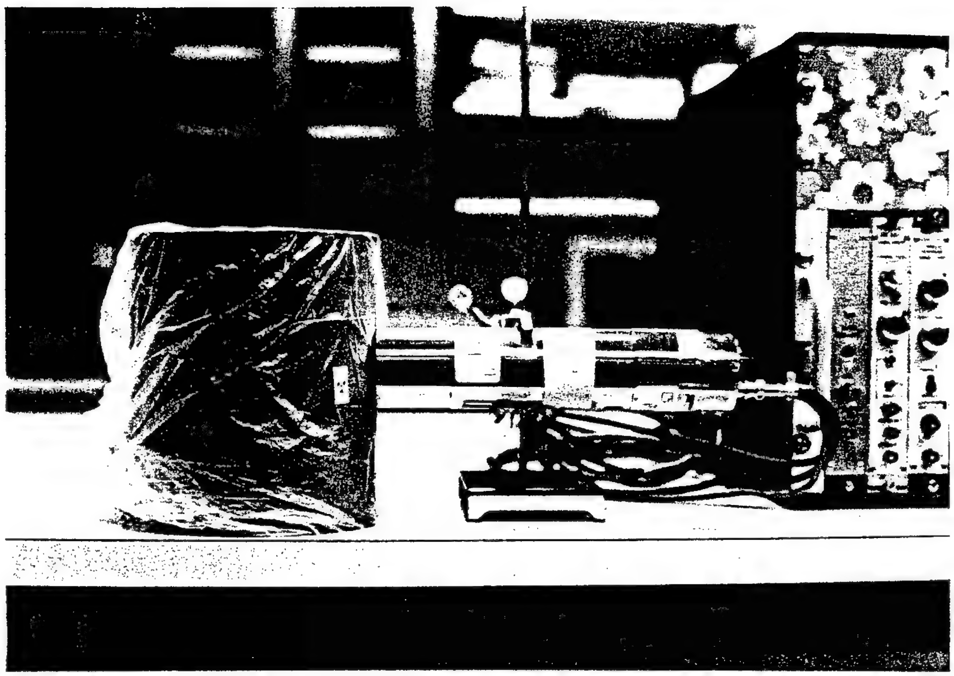

Figure 3. MCA spectra collection from phantoms with detector face positioned on target surface

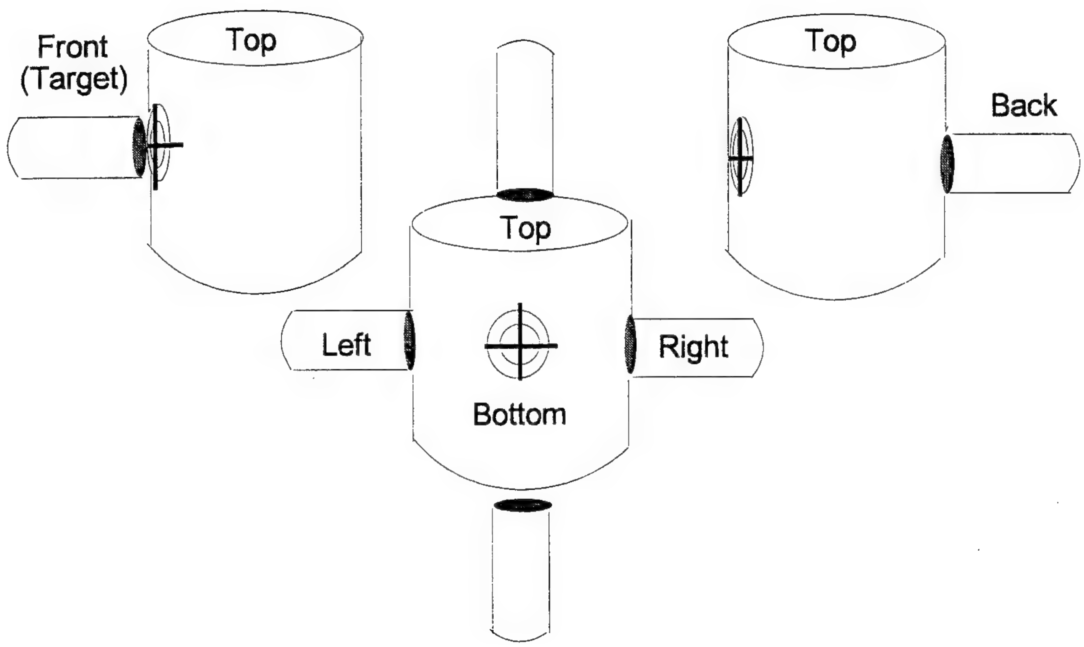

Figure 4. MCA spectra collection from phantoms with the detector face positioned at various positions around the surface of the phantoms

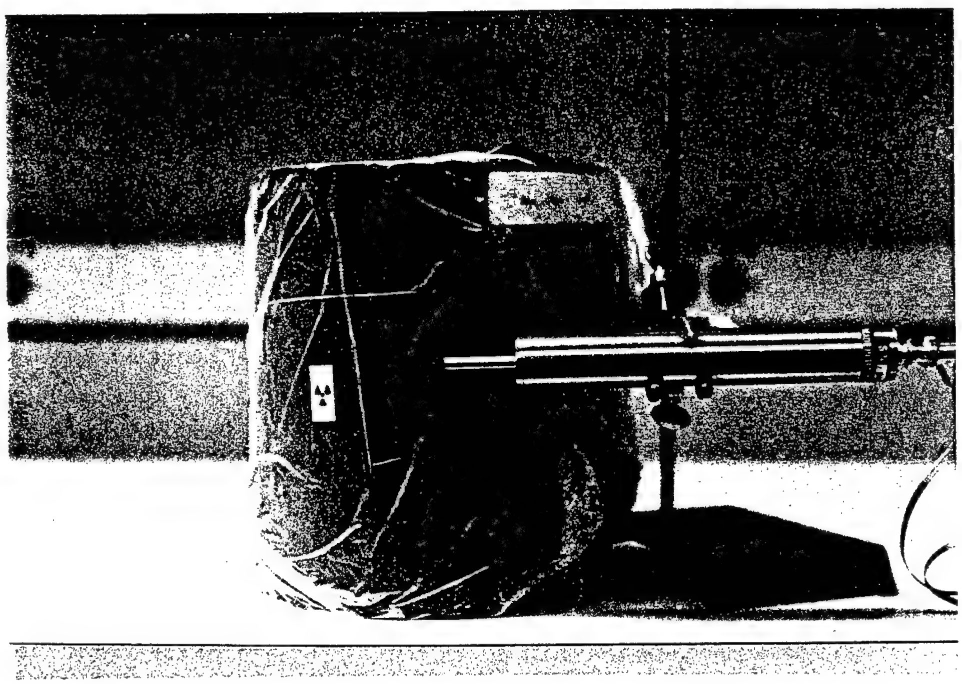

Figure 5. MCA spectra collection from the phantoms using the side of the detectors positioned on the target surface of the phantoms

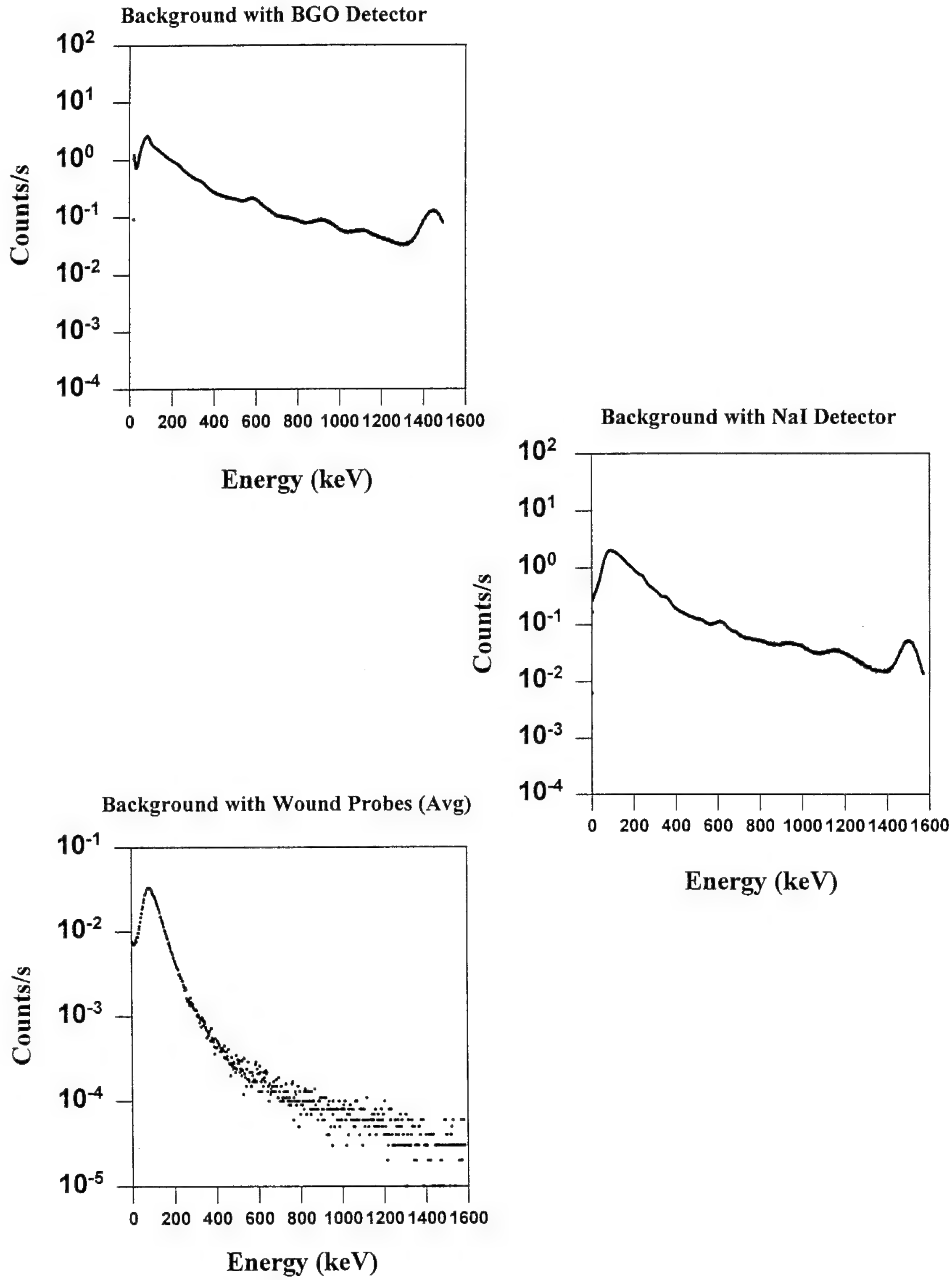

Figure 6. Background spectra from the blank phantom using each detector for long count

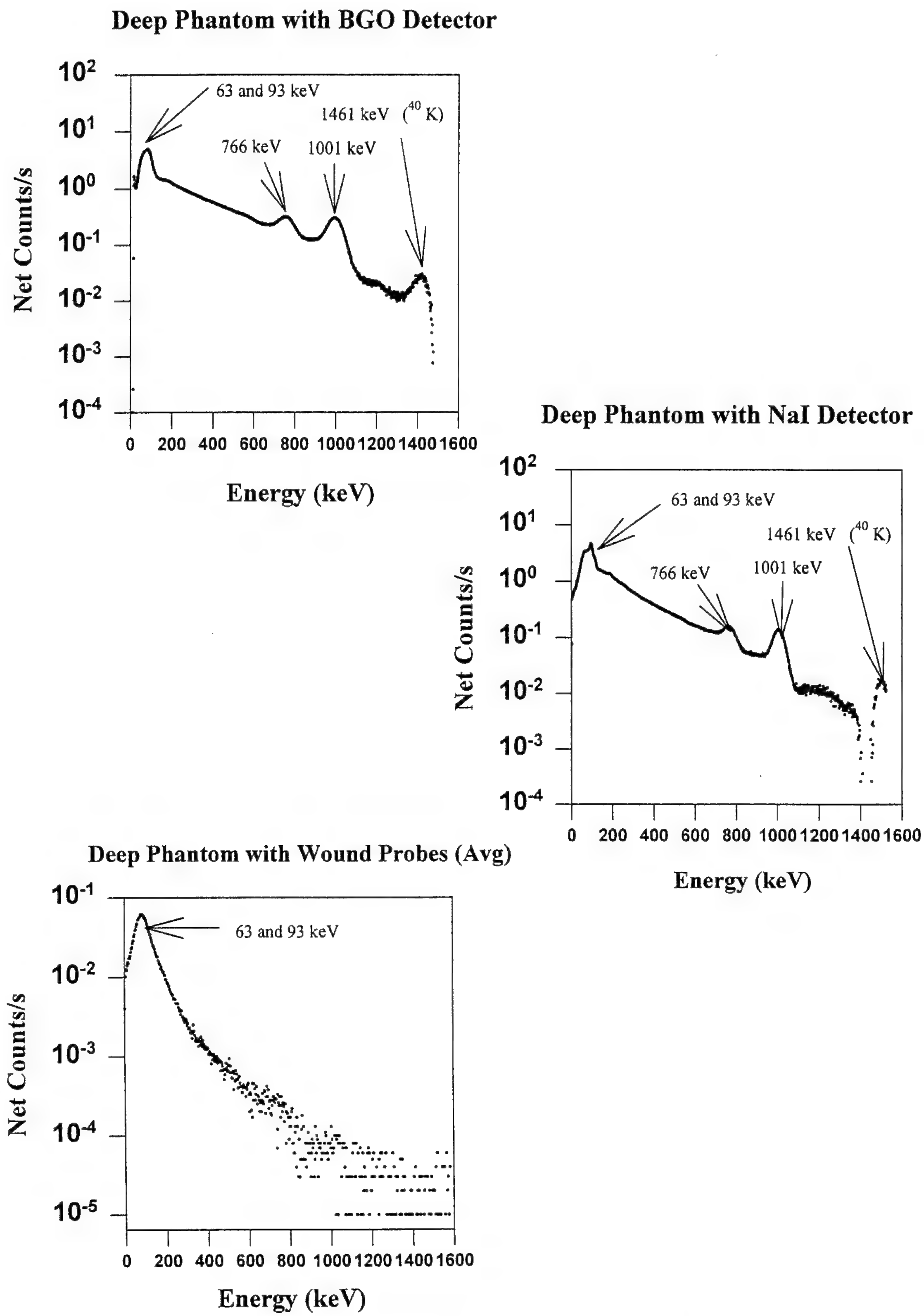

Figure 7. Long count spectra of deep phantom

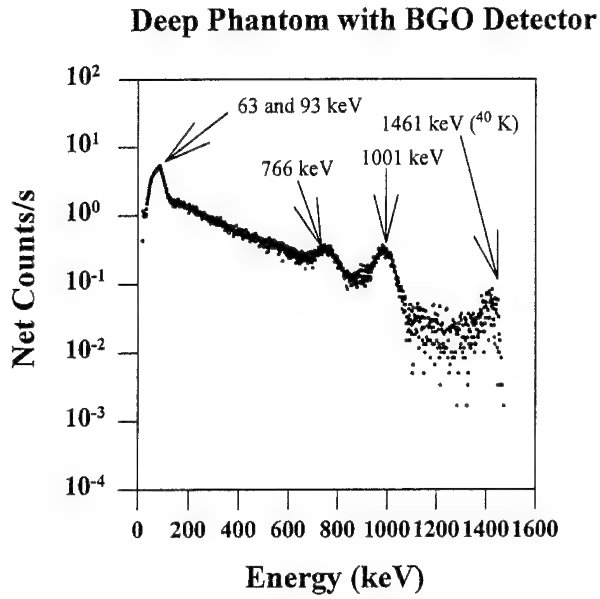

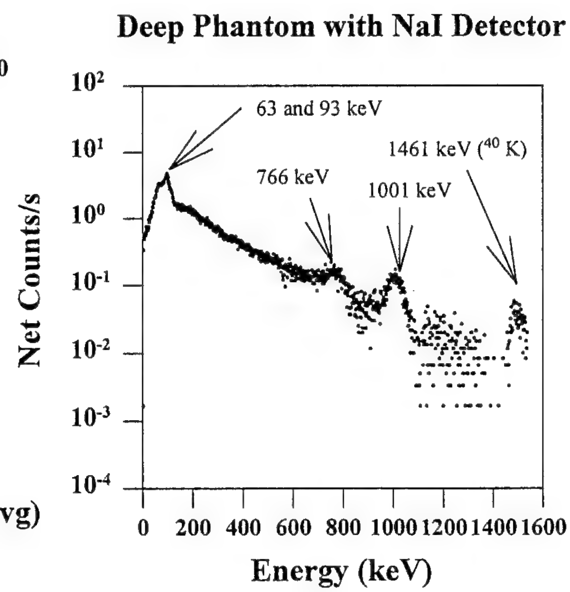

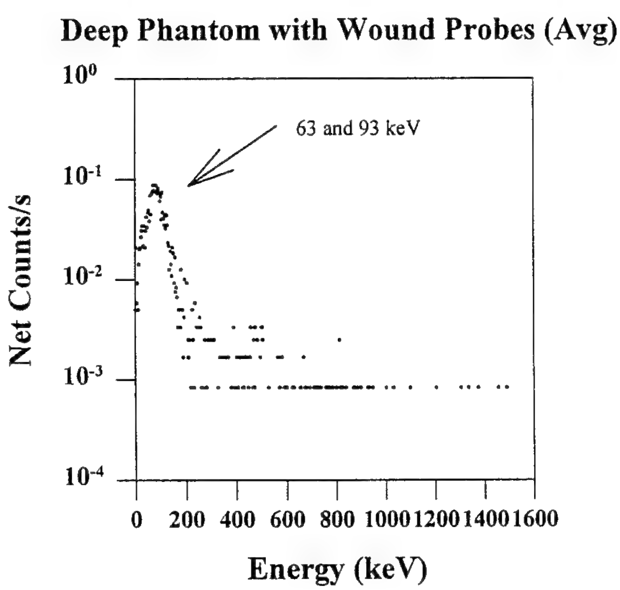

Figure 8. Short count spectra of deep phantom

BGO

NaI

Averaged
Wound
Probes

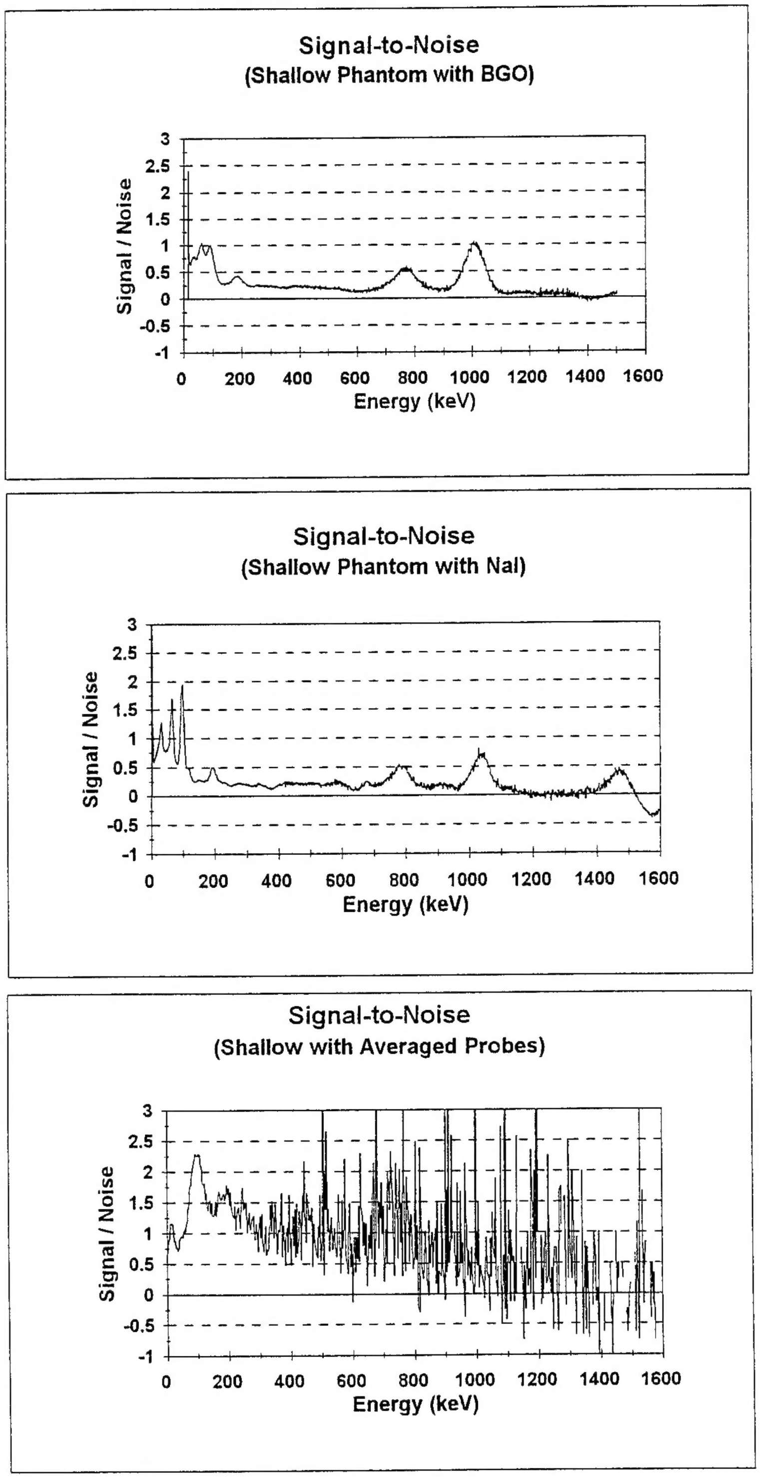

Figure 9. Signal-to-noise ratios for each detector with the shallow phantom

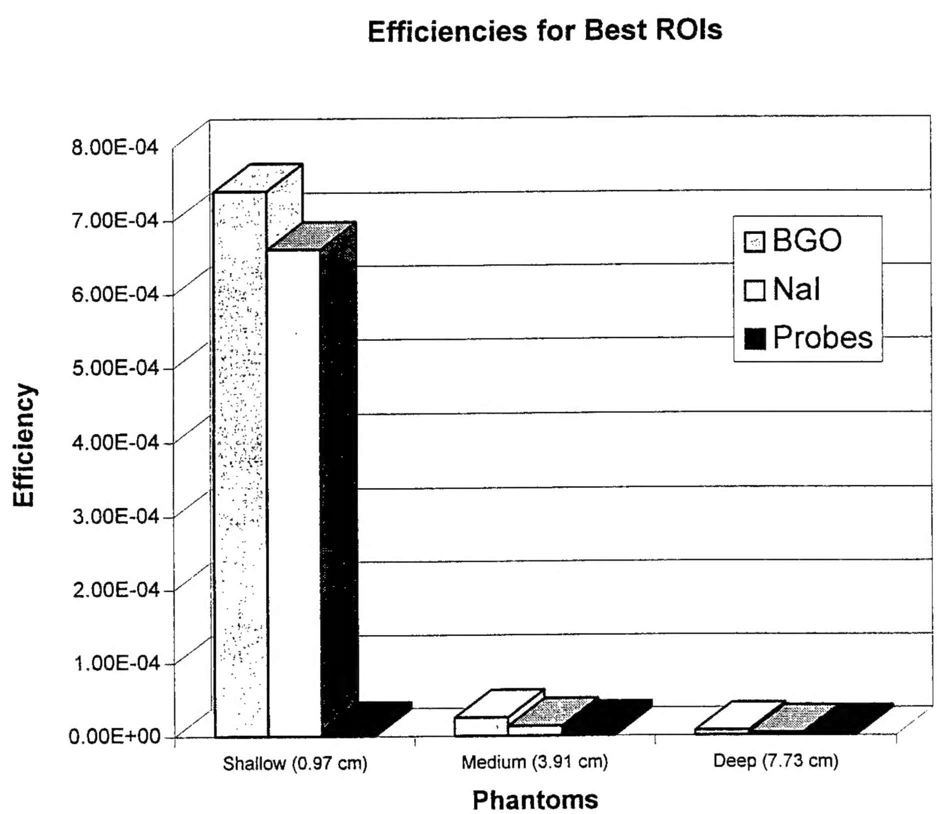

Figure 10. Efficiencies for best ROIs for each phantom (short count)

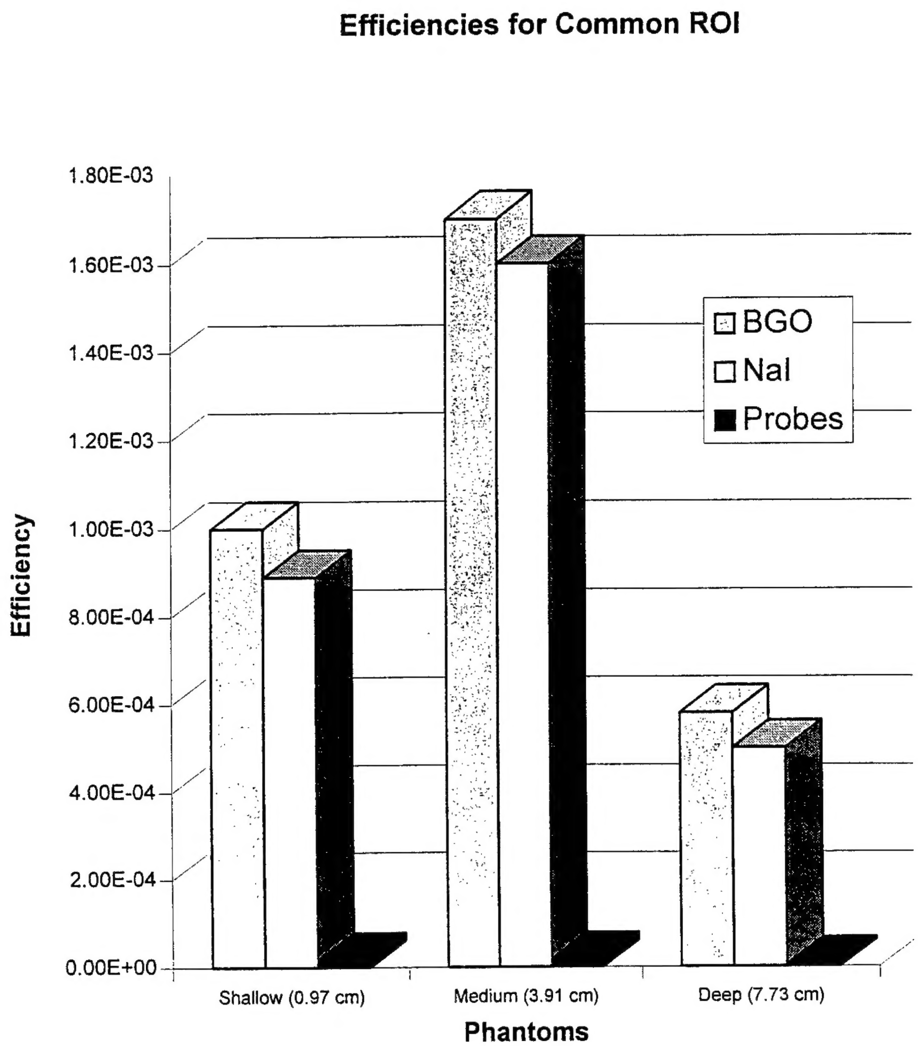

Figure 11. Efficiencies for common ROI for each phantom (short count)

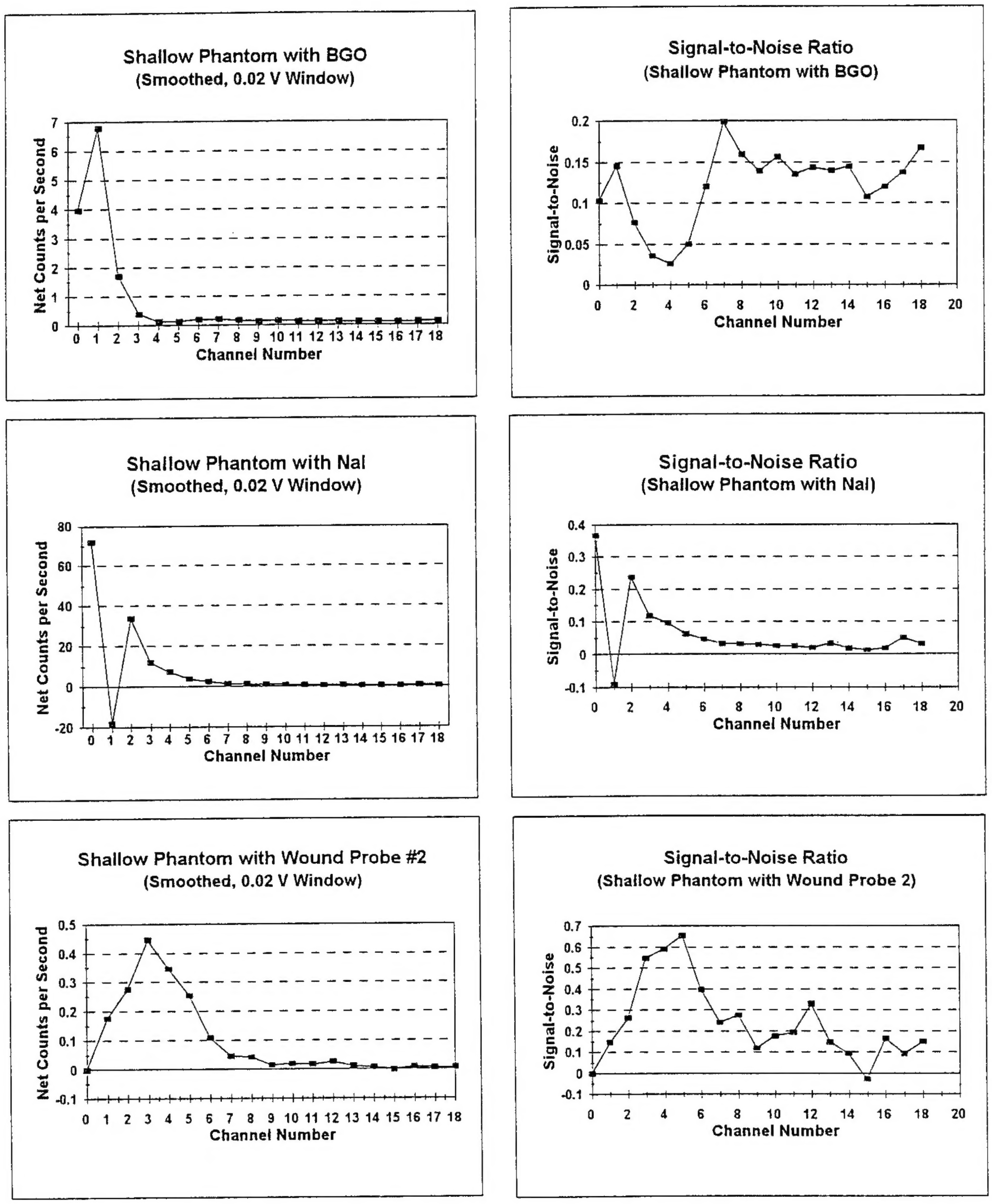

Figure 12. Scaler spectra and signal-to-noise ratios for BGO detector, NaI detector, and wound probe 2